

Contact metamorphism and amphibole-bearing veins in Archean metabasic rocks from the Carajás Mineral Province, northern Brazil

Carlos Eduardo de Mesquita Barros^{1*} , Gláucia Nascimento Queiroga² 

Abstract

In the Carajás Province, many Au and Cu deposits are hosted in Archean metabasic rocks belonging to the Itacaiúnas Supergroup. These metabasic rocks underwent seawater metamorphism of greenschist facies concomitantly to the volcanic activity and banded iron deposition. In the Carajás Province, synkinematic granite magmatism occurred at ca. 2.75 Ga as represented by the Estrela, Serra do Rabo, Planalto, and Igarapé Gelado granites. Emplacement at relatively shallow levels created thermal aureoles of albite-epidote hornfels to hornblende hornfels facies. Metabasic xenoliths show assemblages of hornblende hornfels. Regional stresses and lateral expansion of the syntectonic granites promoted high-temperature low-pressure metamorphism and ductile deformation in the host metabasic rocks. Dehydration reactions increased the fluid pressure permitting hydraulic fracturing and veining in the metabasaltic rocks. These conditions increased the kinetic energy of minerals so that pressure solution and dissolution of minerals were enhanced. The material transfer caused by the advective flow of supersaturated fluids leads to the formation of amphibole-bearing veins and subordinate quartz-bearing and plagioclase-bearing veins. Progressive reactions during thermal metamorphism promoted the replacement of actinolite to ferropargasite/edenite and Na-plagioclase to Ca-plagioclase. Silica produced in these reactions was transported by fluids and deposited in veins that crosscut the amphibolites.

KEYWORDS: Carajás; Archean greenstone belts; contact metamorphism; veining; material transfer.

INTRODUCTION

The mechanisms of space creation during granite plutons emplacement have been debated for decades. Among the different processes that contribute to the ascending and final emplacement of granites, ballooning is responsible for plastic aureole deformation and the final emplacement of plutons (Paterson *et al.* 1991, Weinberg and Podladchikov 1994, Vigneresse and Bouchez 1997, Miller and Paterson 1999). Emplacement of shallow-level granite places side-by-side brittle country rocks metamorphosed under greenschist facies (hydrated assemblages) with plastically deformed counterparts (dry or less hydrated assemblages). The lateral expansion of plutons and aureole deformation, coeval to compressional regional stresses, enhance a rheological change and the plastic flattening of the thermal aureole of country rocks next to the granite intrusion (Bateman 1985, Brun *et al.* 1990). The temperature contrast enhances prograde metamorphism, which controls dehydration reactions and increases fluid pressures, hydraulic fracturing, and veining (Cesare 1994, Davies and

Ferry 1993, Dutrow and Norton 1995, Etheridge *et al.* 1984, Hanson 1992). These conditions are expected in contact metamorphism due to dehydration/devolatilization reactions that occur in previously hydrated rocks (Walther and Orville 1982, Russ-Nabelek 1989, Elmer *et al.* 2006, Yardley and Cleverley 2015). Therefore, discussions on mass transfer mechanisms (Bell and Cuff 1989) and veins formation may contribute to the understanding of the thermal evolution of a terrain (Fischer *et al.* 2019) and may guide the prospection of vein-hosted ore deposits (Bons *et al.* 2012), especially considering the fertile characteristic of Archean greenstone belts (Wang *et al.* 1993).

This paper discusses the origin of amphibole-bearing veins in the context of contact metamorphism in the Carajás Mineral Province (CMP) (Amazon craton) where fertile Archean metabasic rocks are crosscut by synkinematic granites. In this study case, we will present examples of amphibole-bearing veins hosted in metabasic rocks. The discussion is based on field data, petrography, and mineral chemistry.

MATERIALS AND METHODS

The word metabasite is used in a general sense, whereas metabasalts and metagabbros are rocks having primary texture (with blastophitic texture). Amphibolites present massive or foliated structures and granoblastic or nematoblastic textures. To name the amphiboles, we have employed the nomenclature proposed by Leake *et al.* (1997), whereas pyroxenes are named according to Morimoto *et al.* (1988).

¹Universidade Federal do Paraná, Departamento de Geologia – Curitiba (PR), Brazil. E-mail: cadubarros@ufpr.br

²Universidade Federal de Ouro Preto, Departamento de Geologia – Ouro Preto (MG), Brazil. E-mail: glauciaqueiroga@ufop.edu.br

*Corresponding author.



The structures and textures of the metabasic rocks, their location with respect to the synkinematic granites, and the zoning (*cf.* Laird and Albee 1981) in amphibole crystals were crucial to understanding the tectonometamorphic evolution of these amphibolites and the origin of amphibole-bearing veins, albite aggregates and veins of quartz.

The mineral chemistry data were obtained in 23 samples of metabasic rocks. The mineral analyses were carried out in the Microanalysis Laboratory of the University of Lorraine, Nancy (France) with a Cameca SX 50 microprobe equipped with four wavelength dispersive spectrometry (WDS) detectors, under these conditions: 10 A current, 15 kV voltage, and 10 s counting time beam diameter. The THERMOCALC 3.33 program (Powell and Holland 1988, 1994) permitted the calculation of average temperatures and pressures. For such estimating values, one has employed mineral chemical data of a garnet-biotite amphibolite, which is located 400 m away from the contact with the Estrela Granite Complex (CAP 3). For these temperature calculations, the error is furnished by the program as “sigfit” whose value must be smaller than indicated when calculations are finished.

Amphibole compositions were determined from 252 analyses. However, we present the more representative ones for each rock texture variation. Fe_2O_3 values were calculated from the FeO analyses. In the “Results” section, we present the representative mineral chemistry analyses from the metabasites according to textural variation and distance from the synkinematic granite plutons. For pressure calculations, we have tentatively employed the geobarometer amphibole-chlorite proposed by Laird (1991) for rocks that underwent low-grade metamorphism. The chosen sample for the pressure estimating is a metaltramafic schist. The pressure values were calculated with the Eq. 1:

$$P(\text{kbar}) = 10.5 \ln \left[\frac{(Mg/Fe)_{act}}{(Mg/Fe)_{chl}} \right] \quad (1)$$

GEOLOGICAL SETTING

The CMP, which is situated in the SE Amazon craton (Almeida *et al.* 1981), is a notable worldwide known region due to the importance of its ore resources (Fig. 1A). In the CMP, the Mesoarchean basement (Fig. 1B) comprises charnockitic

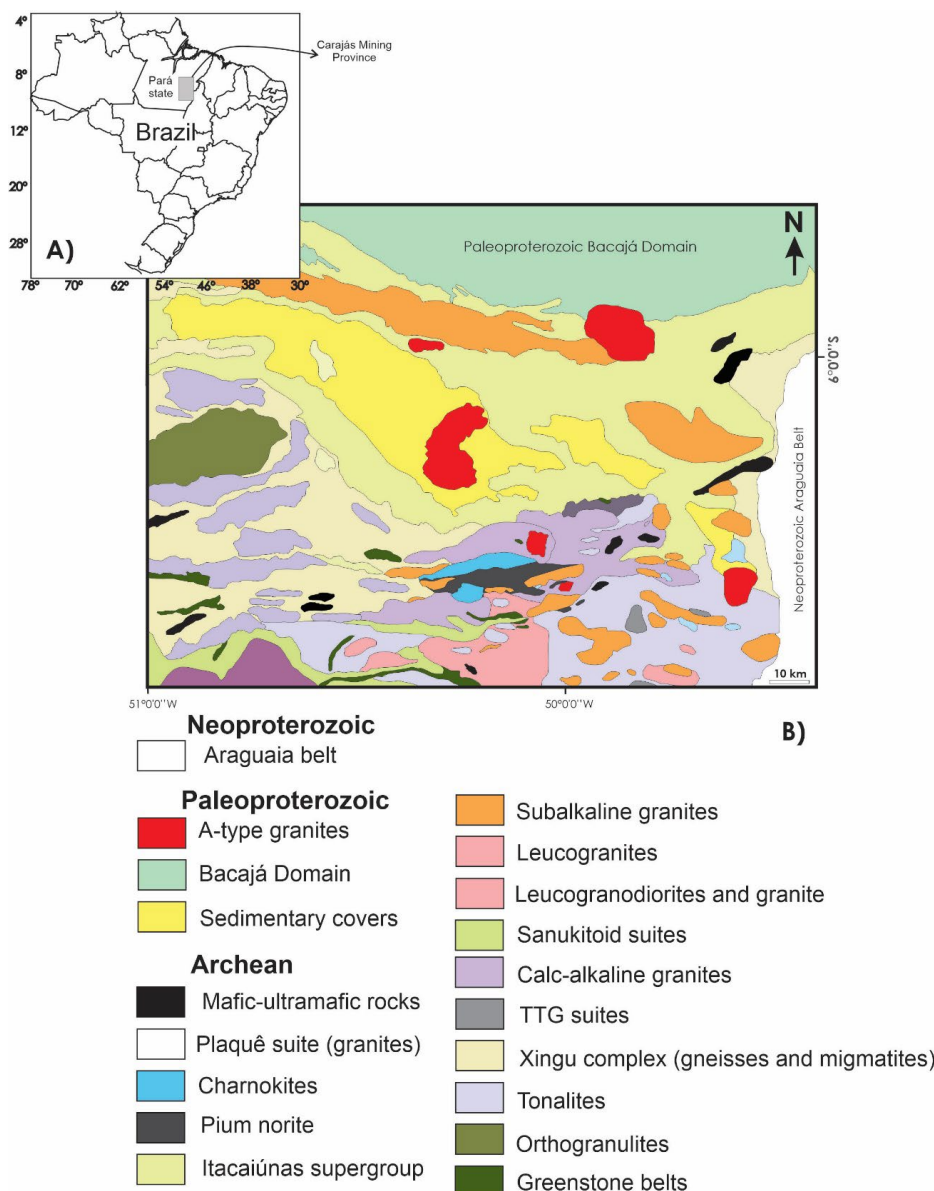


Figure 1. (A) Location map of the Carajás Mining Province. (B) Geological map of the Carajás Mining Province (after Dall’Agnol *et al.* 2017).

to enderbitic gneisses of the Chicrim-Cateté Orthogranulite (3002 ± 14 Ma; Pidgeon *et al.* 2000, Machado *et al.* 1991), tonalitic to trondhjemitic gneisses and migmatites of the Xingu Complex (2974 ± 15 Ma; Avelar *et al.* 1999; 2932 ± 20 Ma; Silva *et al.* 2021), and greenstone belt fragments (2968 ± 15 Ma; Moreto *et al.* 2015). It is also intruded by Mesoarchean granitoids of ca. 3.0 to 2.8 Ga (*e.g.*, Canaã dos Carajás, Bom Jesus, Cruzadão and Bacaba; Moreto *et al.* 2011, Feio *et al.* 2013).

Over this basement, a large Archean basin was formed and covered supracrustal rocks, now represented by basic to felsic metavolcanic rocks, banded iron formations, metapelites, and quartzites (Itacaiúnas Supergroup) (Beisiegel *et al.* 1973, Docegeo 1988, Olszewski *et al.* 1989). U-Pb zircon ages obtained from metabasalts and rhyolites vary from 2774 to 2748 Ga (Wirth *et al.* 1986, Olszewski *et al.* 1989, Machado *et al.* 1991, Tallarico *et al.* 2005, Toledo *et al.* 2019). According to Toledo *et al.* (2019), the age of 2.77 Ga records a tectonometamorphic event on the supracrustal rocks. These supracrustal rocks underwent greenschist metamorphism and a further event of high-temperature and low-pressure (HT/LP) (750°C and ~ 2 kbar) conditions (Lindenmayer *et al.* 1994). Rare cordierite-anthophyllite rocks described in the region were attributed to HT/LP metamorphism on previously altered metabasites (Docegeo 1988).

At the south of the Itacaiúnas Supergroup, major plastic shear zones have been described and attributed to several phases of tectonic reactivation (Pinheiro and Holdsworth 1997). This transpressive structure represents an important mineralized corridor. The supracrustal rocks are cut by

pre-1888 Ma brittle-ductile strike-slip fault (Carajás Fault). Voluminous data have been produced on the ore deposits origin in this part of the worldwide known CMP, where several iron oxide copper gold and volcanogenic massive sulfide ore deposits are described (Schwarz and Frantz 2013, Moreto *et al.* 2015, Hunger *et al.* 2018, Craveiro *et al.* 2019).

The Itacaiúnas Supergroup is crosscut by 2760 to 2743 Ma synkinematic granites (Barros *et al.* 2001, 2009) which show a WNW elongated shape (Fig. 1B). Among these granitic plutons, several bodies are distinguished: Estrela (Fig. 2), Serra do Rabo, Igarapé Gelado, and Planalto. Some of these intrusions have A-type chemical signature and they would have been crystallized from hot magmas produced by partial melting of dry crustal sources (Barros *et al.* 2009). These granitoids show igneous layering, subsolidus magmatic foliation, and syn-emplacment hot mylonites (Barros *et al.* 2001) which testify the thermal signature of decreasing temperatures and increasing deformation during cooling (Barros *et al.* 2001, 2009). The presence of pegmatites showing graphic texture and amphibole with sieve texture in granites suggests the shallow level of emplacement to these plutons (Candela 1997). Because of elevated iron contents in amphibole from the synkinematic granites, the pressure calculations produce overestimated pressure values (Barros *et al.* 2001, 2009, Sardinha *et al.* 2006).

Anorogenic granites (*e.g.*, Central de Carajás and Cigano plutons) of 1888 Ma intruded the Archean rocks (Machado *et al.* 1991, Macambira and Lafon 1995) and Paleoproterozoic sandstones from the Águas Claras Formation (Fabre *et al.* 2011) as discordant batholiths (Fig. 1). These granites have

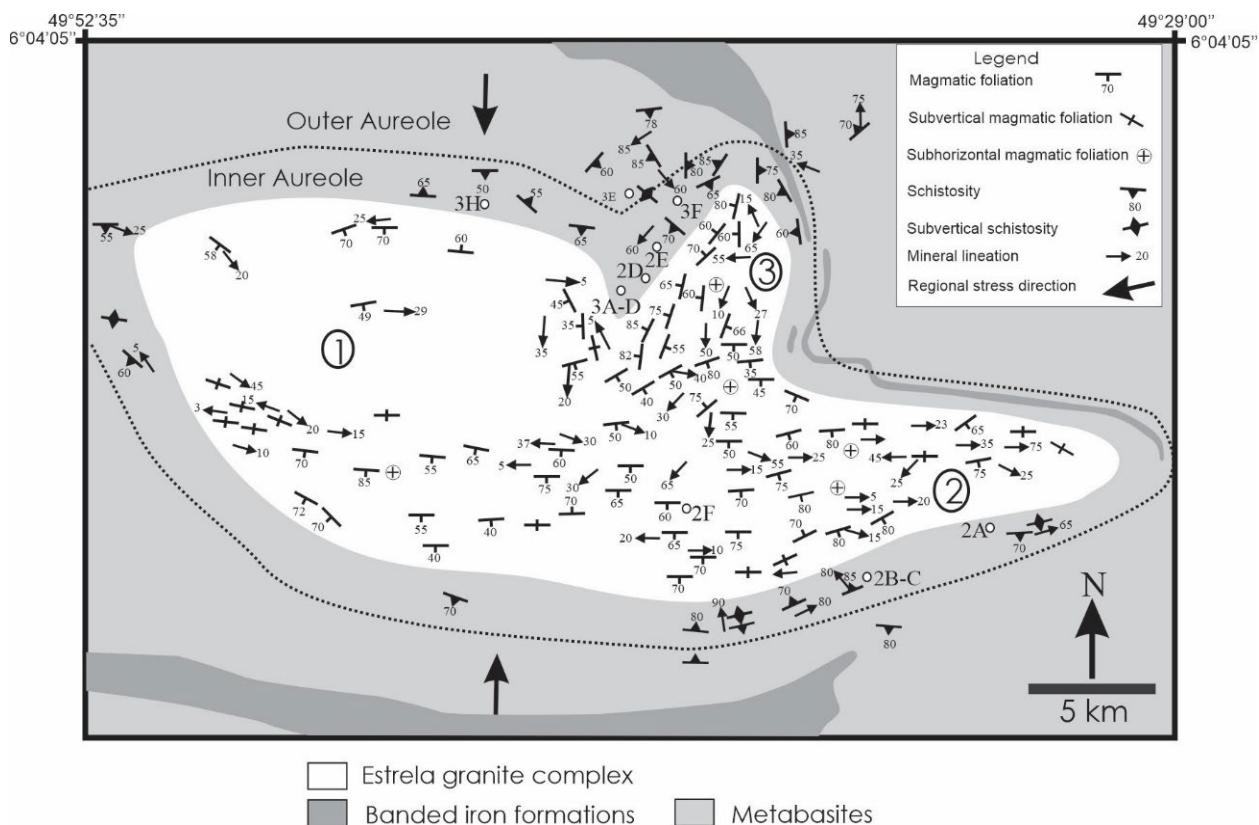


Figure 2. Geological map of the Estrela granite complex and its country rocks. Numbers 1, 2, and 3 indicate plutons that constitute the granite complex. Black dots are outcrop locations of analysis samples, samples mentioned in the text and shown in some figures.

crustal A-type signature, massive structure, and local rapakivi texture (Dall'Agnol *et al.* 1994).

RESULTS

The Itacaiúnas Supergroup is predominantly composed of metabasalts, amphibolites, banded iron formation belts, and minor ultramafic schists. Metagabbros are locally found and spatially associated with the metabasalts, both having iron-rich tholeiitic signature.

The spatial relationship between metabasic rocks and 2.76 to 2.74 Ga synkinematic granites leads to the discrimination of four domains: the outer aureole, the transition domain, the inner aureole, and the xenoliths, where structural, textural, and mineralogical differences are noted and described below.

The inner aureole is around 2 km wide and it comprehends the domain located closer to the Archean 2.76 to 2.74 Ga

synkinematic granites. There, these metabasites underwent HT/LP metamorphism.

Outer aureole

The beginning of the outer aureole is located approximately 4.0 km away from the 2.76 to 2.74 Ga synkinematic granites. The boundary between the outer aureole and the inner aureole is nearly 1.5–2.0 km far from the contact with the synkinematic granites (Fig. 2).

The fine-grained metabasalts and subordinated medium- to coarse-grained metagabbros that belong to the outer aureole (Figs. 2 and 3A) are characterized by dark gray color, massif structure, generalized blastophitic texture, and assemblage composed of actinolite, epidote, and chlorite, which indicates greenschist assemblage (Fig. 4A). Pseudomorphic pale green amphibole replaced primary clinopyroxene. Locally, metabasites are crosscut by a WNW steeply dip foliation (S_1) outlined by low-temperature minerals (chlorite and biotite). In these

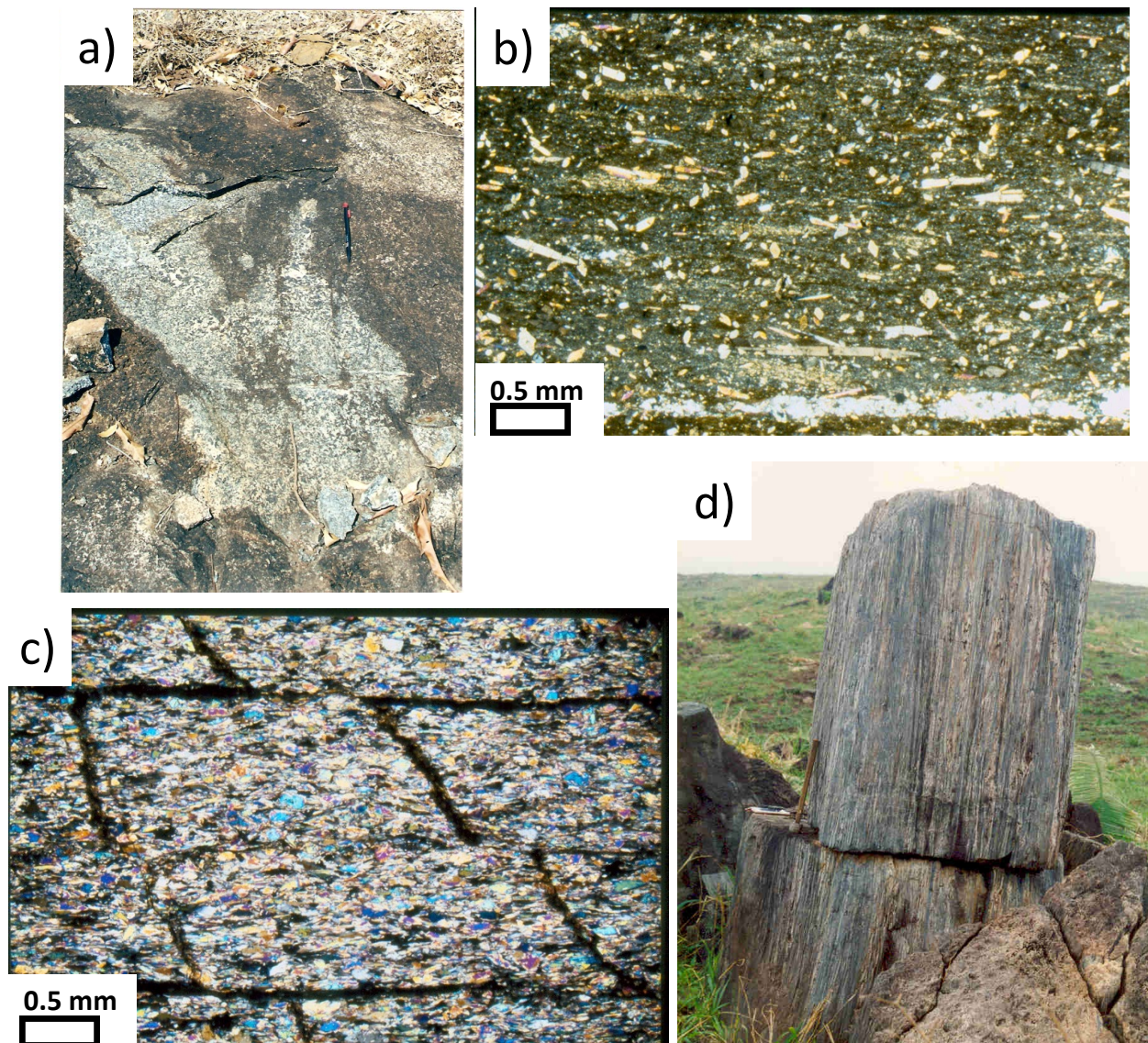


Figure 3. (A) Outcrop of an Archean isotropic metagabbro from the Carajás Mineral Province (outer aureole) (see in the geological map the outcrop CD62 location). (B) Photomicrograph (crossed polarizers) of ultramafic schist from the transition between the outer and inner aureoles. The S_1 schistosity is defined by the strong preferred orientation of chlorite and biotite. Note the tremolite prophyroblasts evidencing the thermal effect. (C) Photomicrograph (crossed polarizers) of a tremolite schist from the inner aureole (S_2). (D) Strongly foliated (S_2) amphibolite from the inner aureole (see in the geological map the outcrop CD52 location).

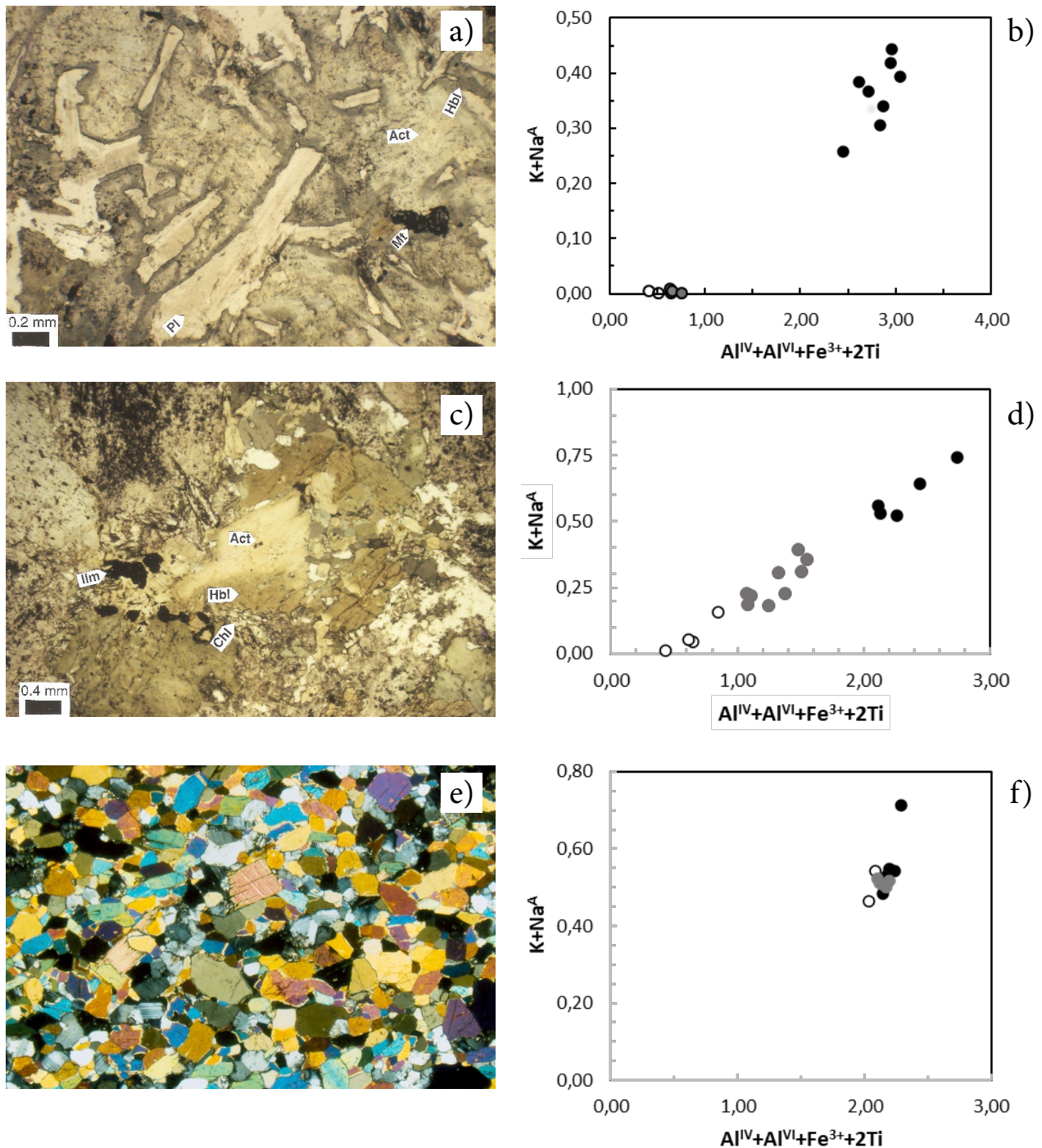


Figure 4. (A) Scanning electronic microscope image of blastophitic metabasalt from the outer aureole (CD22). Note the light gray margins and the dark gray cores of zoned amphibole crystals. (B) Photomicrograph (parallel polarizers) contrasted zoning of amphibole is demonstrated in the $Al(IV)+Al(VI)+Fe(3+)+2Ti$ vs. Site A diagram. (C) Metabasalt from the transition outer aureole-inner aureole (CD61). Note the less contrasted zoning in amphibole. (D) $Al(IV)+Al(VI)+Fe(3+)+2Ti$ vs. Site A. (E) Photomicrograph (crossed polarizers) of massive amphibolite (xenolith) showing granoblastic texture. Note that amphibole is not zoned. (F) $Al(IV)+Al(VI)+Fe(3+)+2Ti$ vs. Site A diagram of massive amphibolite. Black circle indicates crystal margin; gray circle indicates intermediate position; and white circles indicate crystal nuclei (CAP26).

rocks, amphibole (Table 1) has a well-defined chemical and optical zoning (Figs. 4A and 4B) defined by cores of pale green actinolite ($X_{Mg} = 0.541-0.694$) that contrast with the bluish-green to olive green margins of magnesiohornblende or ferropargasite ($X_{Mg} = 0.34-0.46$). This contrasted zoning is well marked by variations of Al, Fe, Ti, Na, and K contents

(Fig. 4B). Plagioclase may preserve its primary lath shape and the oscillatory zoning. Saussuritization of plagioclase is variable but more pronounced in the grain core. Less altered plagioclase preserves the primary composition and zoning (An_{75} core and An_{40} rims) (Table 2). Corroded skeletal magnetite displays some preserved trellis array. Fine quartz

Table 1. Representative chemical analyses of amphiboles from the metabasic rocks and amphibolites that host the Estrela granite complex.

Blastophitic metabasites (outer aureole)									
	CD 22 c	CD 22 i	CD 22 m	CD 65 m	CD 65 c	CD 65 i	CD 65m	CD 65m	
	Actinolite	Ferro tschermakite	Ferro tschermakite	Ferro pargasite	Actinolite	Actinolite	Ferro hornblende	Ferro pargasite	
SiO ₂	53.24	42.52	39.52	40.97	51.61	49.07	43.64	40.48	
TiO ₂	0.12	0.33	0.40	0.25	0.14	0.18	0.23	0.59	
Al ₂ O ₃	2.86	14.05	16.35	12.07	3.47	5.89	10.96	13.32	
FeO	12.27	17.83	18.04	21.37	17.12	17.22	20.85	21.95	
MgO	15.68	8.42	6.51	7.05	12.53	11.60	7.78	6.47	
MnO	0.02	0.33	0.04	0.19	0.52	0.32	0.26	0.22	
CaO	11.96	11.91	11.62	11.63	11.65	11.59	11.56	11.15	
Na ₂ O	0.24	1.23	1.59	1.44	0.46	0.68	1.17	1.62	
K ₂ O	0.00	0.47	0.68	0.78	0.24	0.26	0.43	0.93	
Total	96.63	97.12	95.13	96.01	97.75	97.01	96.98	96.85	
Si	7.692	6.392	5.891	6.367	7.522	7.192	6.654	6.276	
Ti	0.013	0.037	0.045	0.030	0.015	0.019	0.026	0.069	
Al ^{IV}	0.308	1.608	2.109	1.633	0.478	0.808	1.346	1.724	
Al ^{VI}	0.179	0.881	0.763	0.577	0.118	0.209	0.624	0.710	
Fe ³⁺	0.000	0.155	0.000	0.369	0.000	0.000	0.214	0.177	
Fe ²⁺	1.491	2.086	2.345	2.408	2.111	2.149	2.445	2.669	
Mn	0.003	0.005	0.025	0.025	0.064	0.040	0.034	0.029	
Mg	3.378	1.886	1.447	1.632	2.721	2.534	1.768	1.495	
Ca	1.852	1.919	1.855	1.936	1.819	1.820	1.888	1.851	
Na ^{M4}	0.066	0.081	0.145	0.064	0.130	0.180	0.112	0.149	
Na ^A	0.000	0.278	0.314	0.369	0.000	0.014	0.235	0.338	
K	0.000	0.089	0.129	0.155	0.044	0.049	0.083	0.184	
XMg	0.694	0.457	0.382	0.370	0.563	0.541	0.399	0.344	
Foliated amphibolites (inner aureole)									
	CAP 8 m	CAP 8 i	CAP 8 i	CAP 8 c	CAP15m	CAP15m	CAP15c	CAP 15i	CAP 15c
	Ferro tschermakite	Ferro pargasite	Ferro pargasite	Ferro pargasite	Mg hbl	Mg hbl	Mg hbl	Mg hbl	Mg hbl
SiO ₂	41.88	41.98	42.11	42.22	48.62	47.28	48.29	46.79	48.12
TiO ₂	1.35	1.26	1.28	1.13	0.58	0.55	0.46	0.51	0.46
Al ₂ O ₃	9.42	9.49	9.65	9.80	8.14	8.91	7.75	8.80	7.78
FeO	22.80	23.44	22.56	23.05	14.96	15.56	14.92	16.79	16.20
MnO	0.00	0.01	0.14	0.08	0.11	0.14	0.08	0.06	0.15
MgO	6.94	6.99	7.13	6.83	11.88	11.45	11.88	10.86	11.86
CaO	10.70	11.09	11.24	11.29	12.15	11.89	12.03	11.74	11.80
Na ₂ O	1.76	1.79	1.77	1.79	0.81	0.77	0.82	0.84	0.73
K ₂ O	1.35	1.22	1.26	1.46	0.30	0.42	0.31	0.58	0.36
Total	96.21	97.27	97.14	97.74	97.55	96.97	96.54	96.97	98.16
Structural formula (23 oxygens and 15 cations)									
Si	6.281	6.558	6.245	6.230	7.017	6.875	7.040	6.990	7.064
Ti	0.152	0.148	0.143	0.125	0.063	0.060	0.050	0.057	0.051
Al ^{IV}	1.665	1.442	1.687	1.704	0.983	1.125	0.960	1.010	0.936
Al ^{VI}	0.000	0.305	0.000	0.000	0.402	0.402	0.371	0.540	0.410
Fe ³⁺	0.000	0.056	0.000	0.000	0.000	0.000	0.000	0.001	0.069
Fe ²⁺	3.014	3.006	2.945	3.003	1.840	1.930	1.855	2.096	1.920
Mn	0.000	0.001	0.018	0.010	0.013	0.017	0.010	0.008	0.019
Mg	1.551	1.628	1.576	1.502	2.556	2.482	2.581	2.418	2.595
Ca	1.719	1.856	1.786	1.785	1.879	1.852	1.879	1.879	1.856
Na ^{M4}	0.281	0.144	0.214	0.215	0.121	0.148	0.121	0.121	0.144
Na ^A	0.231	0.398	0.295	0.297	0.105	0.069	0.111	0.123	0.064
K	0.258	0.243	0.238	0.275	0.055	0.078	0.058	0.111	0.067
XMg	0.340	0.351	0.349	0.333	0.581	0.563	0.582	0.537	0.575

Continue...

Table 1. Continuation.

Sample	Garnet-biotite amphibolite (inner aureole)				Amphibolite (xenolith)			
	CAP 3c	CAP 3c	CAP 3i	CAP 3m	CN39i	CN39m	CN39m	CN39c
	Ferro tschermakite	Ferro tschermakite	Ferro tschermakite	Ferro tschermakite	Ferro tschermakite	Ferro tschermakite	Ferro pargasite	Ferro edenite
SiO ₂	39.98	40.17	41.23	40.66	42.72	42.30	42.19	42.03
TiO ₂	0.47	0.34	0.42	0.34	1.51	1.65	1.61	1.31
Al ₂ O ₃	16.21	16.47	15.52	16.10	11.13	11.28	11.23	9.92
FeO	20.75	20.30	19.32	20.06	18.53	19.15	19.47	18.97
MnO	0.16	0.00	0.00	0.04	0.18	0.22	0.16	0.22
MgO	6.47	6.57	7.13	6.58	8.37	7.59	7.80	8.67
CaO	10.58	10.45	10.85	10.57	11.61	11.50	11.53	11.66
Na ₂ O	1.50	1.34	1.45	1.32	1.80	1.72	1.83	1.49
K ₂ O	0.27	0.33	0.32	0.34	0.84	0.91	0.95	0.91
Total	96.36	96.03	96.40	96.05	96.78	96.40	96.83	95.31
Structural formula (23 oxygens and 15 cations)								
Si	6.125	6.159	6.087	6.233	6.272	6.268	6.214	6.551
Ti	0.054	0.039	0.047	0.039	0.167	0.184	0.178	0.154
Al ^{IV}	1.875	1.841	1.913	1.767	1.728	1.732	1.786	1.449
Al ^{VI}	1.052	1.135	0.788	0.141	0.198	0.238	0.163	0.373
Fe ³⁺	0.216	0.155	0.000	0.083	0.000	0.000	0.000	0.115
Fe ²⁺	2.443	2.448	2.467	2.489	2.383	2.485	2.516	2.358
Mn	0.021	0.000	0.000	0.000	0.022	0.028	0.020	0.029
Mg	1.477	1.501	1.569	1.503	1.832	1.676	1.712	2.014
Ca	1.737	1.717	1.716	1.736	1.970	1.826	1.820	1.947
Na ^{M4}	0.263	0.283	0.284	0.264	0.174	0.174	0.180	0.373
Na ^A	0.182	0.115	0.131	0.128	0.339	0.320	0.342	0.397
K	0.053	0.065	0.060	0.066	0.157	0.172	0.178	0.181
XMg	0.357	0.366	0.389	0.369	0.435	0.403	0.405	0.449

c: core; i: intermediate; m: margin.

Table 2. Representative chemical analyses of diopside from the massive amphibolites (xenoliths).

	Clinopyroxene amphibolite (xenoliths)								
	CRN32c	CRN32m	CRN32m	CRN32i	CN39m	CN39i	CN39c	CN 39i	CN 39c
SiO ₂	52.15	51.78	52.46	52.91	52.92	52.55	52.86	53.11	53.09
TiO ₂	0.06	0.12	0.02	0.09	0.06	0.10	0.04	0.01	0.07
Al ₂ O ₃	0.68	0.66	0.70	0.79	0.59	0.49	0.50	0.50	0.48
FeO	12.48	12.51	12.84	11.27	11.6	11.61	10.61	10.84	11.20
MnO	0.46	0.36	0.36	0.57	0.15	0.31	0.17	0.18	0.26
MgO	10.93	10.98	12.26	10.99	12.07	11.93	12.11	11.87	11.90
CaO	22.87	23.29	22.84	23.91	22.90	22.68	22.97	22.72	22.92
Na ₂ O	0.17	0.19	0.23	0.23	0.18	0.09	0.16	0.16	0.25
K ₂ O	0.00	0.00	0.00	0.00	0.01	0.00	0.00	0.03	0.00
Total	99.84	100.04	100.77	100.76	100.49	99.87	99.46	99.47	100.23
Structural formula (six oxygens)									
Si	1.987	1.968	1.978	1.992	1.990	1.992	2.004	2.017	2.001
Ti	0.002	0.003	0.001	0.003	0.002	0.003	0.001	0.000	0.002
Al ^{IV}	0.013	0.030	0.022	0.008	0.000	0.008	0.000	0.000	0.000
Al ^{VI}	0.018	0.000	0.009	0.027	0.021	0.014	0.022	0.022	0.021
Fe ³⁺	0.003	0.040	0.027	0.000	0.000	0.000	0.000	0.000	0.000
Fe ²⁺	0.355	0.334	0.329	0.336	0.300	0.299	0.287	0.300	0.300
Mn	0.015	0.012	0.011	0.018	0.000	0.010	0.005	0.006	0.008
Mg	0.621	0.622	0.633	0.617	0.669	0.674	0.684	0.672	0.669
Ca	0.934	0.949	0.923	0.964	0.926	0.921	0.933	0.924	0.926
Na	0.013	0.014	0.017	0.017	0.018	0.007	0.012	0.012	0.018
K	0.000	0.000	0.000	0.000	0.000	0.000	0.000	0.001	0.000
%En	31.56	31.42	32.09	31.56	34.19	34.16	34.93	34.52	34.19
%Fs	20.97	20.67	21.12	19.09	18.48	19.16	17.45	17.99	18.48
%Wo	47.47	47.91	46.79	49.35	47.33	46.68	47.62	47.50	47.33

c: core; i: intermediate; m: margin.

aggregates dispersed in the matrix show relict shapes of the primary graphic texture.

Transition domain

Two kilometers far from the granites in the transition between the outer and inner aureoles, the metabasic rocks present in the assemblage are composed of labradorite (An 54.12–63.01) (Table 2), magnesium-rich chlorite (MgO = 20.29–24.41; FeO = 11.65–20.41), tremolite (XMg = 0.764–0.805), or pale green magnesiohornblende (XMg = 0.627–0.652) (Table 1). Labradorite most probably is a heritage from the primary composition. Blastophitic texture can coexist with localized and weak preferred orientation of minerals that record the initial development of a schistosity. Amphibole crystals exhibit more gradual chemical zoning outlined by pale green actinolite of the core toward the olive green ferropargasite or magnesiohornblende of the intermediate and margins parts (Fig. 4C). This transitional variation is reflected by continuous enrichment in Al, Ti, Fe, Na, and K toward the rims (Fig. 4D). In these transition domains, the metabasalts are affected by 30-cm-wide steeply dip schistosity (S_1) striking E-W. In association with metabasalts, there are rare ultramafic schists characterized by a fine-grained matrix composed of chlorite and biotite, both showing strong preferred orientation (S_1). This matrix is crosscut by tremolite porphyroblasts (Fig. 3B). In places, this schistosity (S_1) is crosscut by amphibole crystals which are laid on the foliated matrix by oriented in different directions. This indicates that the foliation defined by chlorite and biotite (S_1) was formed before the amphibole growth, which would have occurred under weak compressional stress.

In this transition zone, banded iron formations display steeply dip foliation concordant to the contacts with the 2.76 to 2.74 Ga synkinematic granites. The thermal metamorphism in these ironstones is evidenced by coarse-grained muscovite randomly oriented.

Inner aureole

In the 2-km-wide inner aureole (Fig. 2), the foliated amphibolites present strong schistosity (S_2) defined by the preferred orientation of amphibole, plagioclase, and, sometimes, biotite (Figs. 3C and 3D). Foliation is subvertical and concordant with contact with the synkinematic granites. In some places, steep plunging mineral lineation occurs. Besides the western and eastern parts of the Estrela Granite Complex, the schistosity along the host thermally metamorphosed amphibolites display a rather triangular foliation trajectory. The same behavior is observed to the north of the Estrela Granite Complex. There, within the domain of triangular foliation trajectory, one also observes L-tectonites. Foliated amphibolites (CAP 15) have nematoblastic texture, and the boundaries of the crystals are generally straight. Amphibole (Table 1) is olive green magnesiohornblende (XMg ~ 0.57) characterized by the absence of zoning. Amphibole compositions are distinguished by higher Al, Fe, Ti, Na, and K contents when compared with the amphibole compositions of the outer aureole metabasites. Plagioclase is devoid of strong saussurite alteration and its

composition varies from oligoclase to labradorite (An 23–62) (Table 2). Ilmenite occurs as fine lamellar grains that show moderate to strong preferred orientation.

Locally, in the inner aureole, a foliated amphibolite (CAP 8) is distinguished by the assemblage composed of plagioclase (An 43 to 36), ferrotschermakite and ferropargasite (XMg ~ 0.35), cummingtonite, biotite, scapolite, and quartz.

To the south and southeast of the Estrela Granite Complex, an outcrop of foliated garnet-biotite amphibolite (CAP 3), located 400 m away from the contact with the pluton, is distinguished by the presence of very-coarse and numerous garnet porphyroblasts (Fig. 5A). Major-elements analysis of this rock permits to compare its composition to that of the andesite basalt. Curved inclusions of fine-grained aligned ilmenite within the rounded porphyroblasts have continuity outside of the matrix domains. Another manner in which garnet porphyroblast occurs is as an elongated crystal parallel to the schistosity. Besides garnet crystals, quartz is common, or as aggregates or as strain shadows. Amphibole and tourmaline may exhibit dissolution discontinuities orthogonal to the planar structure, giving rise to the tablet-of-chocolate texture (Fig. 5C). Amphibole is pale to olive green ferrotschermakite (XMg ~ 0.38) that shows strong preferred orientation and straight contacts. Plagioclase crystals (An 45–52) are devoid of alteration, display strong preferred orientation, and exhibit straight boundaries. In these wall rocks, the foliation strikes N85E/85NW. It is very strong and defined by the preferred orientation of olive-green amphibole, plagioclase, biotite, \pm tourmaline, and \pm ilmenite. The mineral lineation, which is marked by biotite and amphibole, plunges 85/330. Oriented thin section permitted us to determine that in this southern inner aureole, the rocks experienced an inverse sense of movement from north to south.

Locally, in the inner aureole, foliated amphibolites host meter-wide veins of quartz with associated pyrite. Until recently, from this small mine called Serra Verde, gold had been exploited.

Xenoliths

Within the Estrela Granite Complex, there is a set of amphibolites that may both represent xenoliths and possibly rests of a septum close to the contacts between plutons. These rocks are massif and display granoblastic texture (Fig. 4E), brownish amphibole, or olive-green amphibole \pm clinopyroxene. Locally, these rocks show coarse-grained crystals that have polygonal contacts. Amphibole crystals (Table 1) are not zoned and present high values of Al, Ti, Fe, Na, and K (Fig. 4F). Amphibole varies in composition from ferropargasite to ferrotschermakite (XMg = 0.35–0.45). Clinopyroxene (Table 3) has diopside composition (En = 34.08–34.11%; Fs = 18.48–21.30%; Wo = 47.33–44.58%), may reach 25% of the rocks, and occurs as fine- to medium-grained crystals that show straight contacts. Plagioclase (An 62 to 48) (Table 2) is characterized by a limpid aspect and polygonal crystals. Few biotite crystals are present and distinguished by reddish-brown colors.

A summary of rock types, textures, and mineral compositions is presented in Table 4.

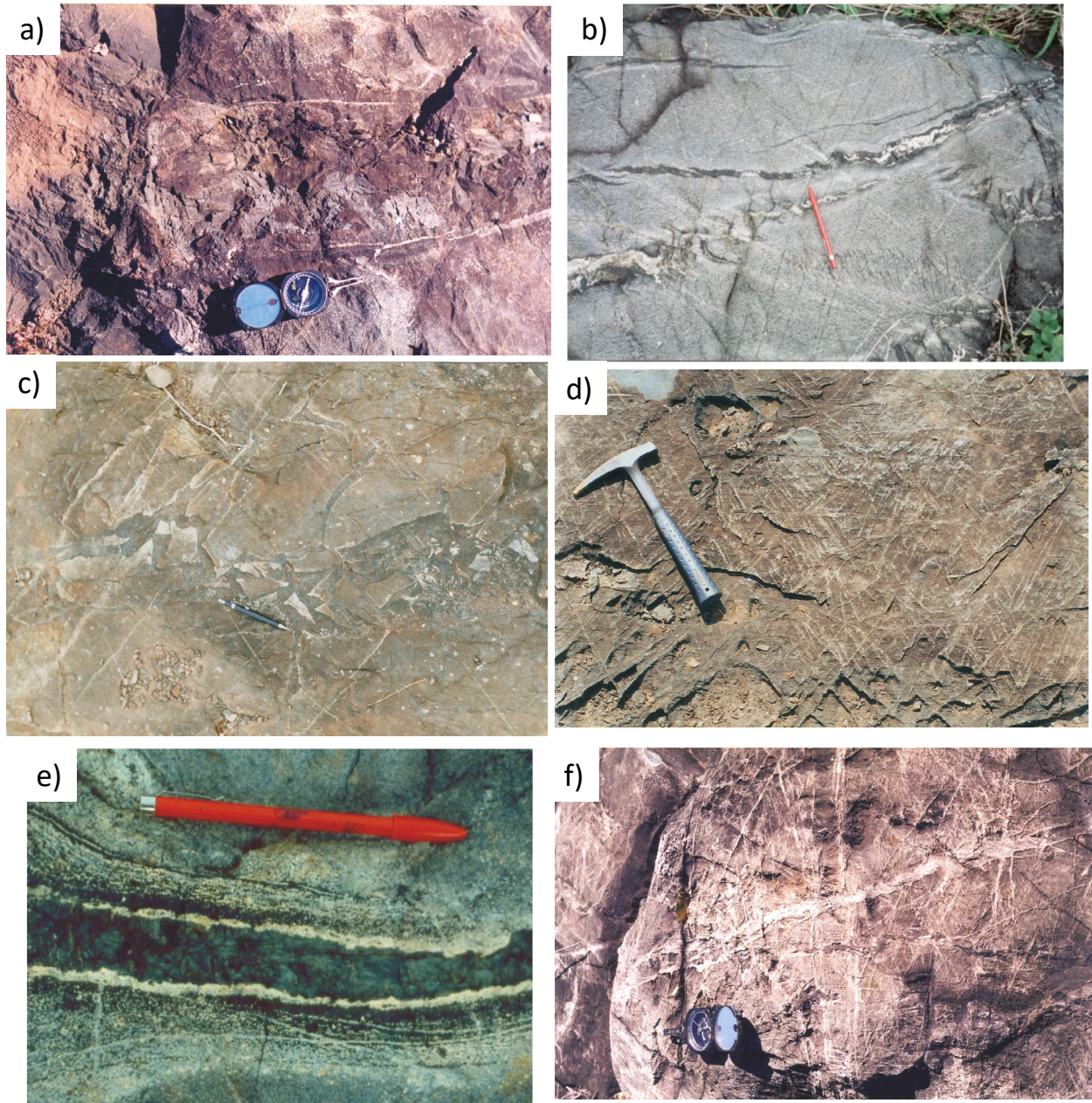


Figure 5. Amphibolites crosscut by amphibole-bearing veins or hydraulic fractures. (A) Amphibolite from the inner aureole crosscut by decimeter-wide amphibole-bearing vein (parallel to the compass). Notice the very coarse-grained amphibole filling the vein (CD20). (B) Amphibolite xenolith crosscut by amphibole- and amphibole-plagioclase-bearing veins. Note some veins in en-échelon array (CAP26). (C) Amphibole-bearing vein showing brecciated aspect (CD20). (D) Conjugated hydraulic fractures (CAP3). (E) Zoned veins filled with amphibole and plagioclase (II29). (F) Multidirectional hydraulic fractures (CAP-10). (All photos were taken in the plant.).

HYDRAULIC FRACTURES AND VEINS

Amphibole-bearing veins, plagioclase veins or aggregates, and veins of quartz are abundant in amphibolites from both inner aureole and the xenoliths. The veins' shapes and their spatial relation with the schistosity developed during the contact metamorphism are described below.

- *Hydraulic fractures and veins orthogonal to the S_2 schistosity* are abundant in the foliated amphibolites from the inner aureole. The veins are filled with coarse-grained and sub-euhedral amphibole. Locally, a 50-cm-wide vein is filled with very coarse-grained 10-cm-long amphibole crystals (Fig. 6A) and shows pegmatitic texture. Most of these amphibole-bearing veins show massive structure, but a few

amphibole crystals can have grown orthogonally to the vein walls. Amphibole composition varies from actinolite to ferropargasite (Table 5). In some veins, two amphibole types are intergrown in a complex array. In general, they are similar to the amphibole of the metabasite that hosts the veins;

- *En échelon veins and fractures* are also found in foliated amphibolites along the inner aureole and in the xenoliths (Fig. 6B);
- *Amphibole-bearing veins with brecciated aspect* (Fig. 6C). In these veins, angular fragments of the host metabasites are enclosed by the coarse-grained amphibole. There, the host-foliated amphibolites may show a whitish-gray color close to the vein walls;

Table 3. Representative chemical data of amphiboles that fill the veins.

Samples	CAP 9	II-29	II-29	CAP 10	CAP 10	CAP 10	CAP 10	CAP 11
	Actinolite	Actinolite	Actinolite	Ferro actinolite	Ferro edenite	Ferro pargasite	Ferro pargasite	Ferro pargasite
SiO ₂	52.57	50.79	50.51	47.90	42.02	42.40	40.72	39.52
TiO ₂	0.04	0.27	0.13	0.24	0.43	0.55	0.32	0.04
Al ₂ O ₃	2.33	3.36	3.78	6.05	10.39	10.57	12.01	12.81
FeO	17.98	19.75	19.06	19.90	22.49	22.46	24.08	24.32
MnO	0.00	0.00	0.18	0.13	0.19	0.09	0.07	0.16
MgO	11.81	11.41	10.89	9.21	6.48	6.29	5.16	5.03
CaO	12.35	11.42	12.12	11.66	11.72	11.50	11.15	11.58
Na ₂ O	0.22	0.97	0.59	1.01	1.42	1.58	1.57	1.70
K ₂ O	0.09	0.37	0.23	0.29	0.99	1.14	1.13	1.31
Total	97.39	98.44	98.09	96.41	96.27	96.58	96.21	96.47
Structural formula (23 oxygens and 15 cations)								
Si	7.749	7.386	7.407	7.147	6.581	6.338	6.433	6.238
Ti	0.004	0.030	0.014	0.027	0.051	0.062	0.038	0.005
Al ^{IV}	0.251	0.576	0.593	0.853	1.419	1.662	1.567	1.762
Al ^{VI}	0.154	0.000	0.060	0.211	0.499	0.200	0.669	0.621
Fe ³⁺	0.000	0.000	0.000	0.000	0.154	0.000	0.114	0.347
Fe ²⁺	2.228	2.460	2.382	2.543	2.791	2.940	3.068	2.864
Mn	0.000	0.000	0.022	0.016	0.025	0.011	0.009	0.021
Mg	2.595	4.473	2.380	2.048	1.513	1.401	1.215	1.183
Ca	1.950	1.779	1.904	1.864	1.967	1.842	1.887	1.958
Na ^{M4}	0.050	0.221	0.096	0.136	0.033	0.158	0.113	0.042
Na ^A	0.013	0.053	0.072	0.156	0.398	0.300	0.368	0.479
K	0.017	0.069	0.043	0.055	0.198	0.217	0.228	0.264
XMg	0.538	0.501	0.500	0.446	0.339	0.323	0.276	0.269

Table 4. Representative chemical data of plagioclase crystals from amphibolites.

	Blastophitic metabasic rocks (outer aureole)							
	CD 22 c	CD 22 c	CD 22 i	CD 22 i	CD 65 c	CD 65 r	CD 65 i	CD 65 r
SiO ₂	50.47	50.24	54.16	53.58	53.39	55.85	58.58	59.19
Al ₂ O ₃	30.28	30.42	23.70	23.93	29.37	27.27	25.81	25.13
TiO ₂	0.00	0.04	0.01	0.00	0.01	0.05	0.00	0.59
FeO	0.74	1.64	0.15	0.14	0.66	0.55	0.19	1.11
MnO	0.00	0.12	0.00	0.02	0.11	0.04	0.00	0.05
MgO	0.27	0.12	0.00	0.00	0.04	0.06	0.00	0.20
CaO	13.26	13.70	9.95	10.25	12.41	9.41	8.05	6.86
Na ₂ O	3.85	3.34	8.13	8.42	4.59	6.08	7.37	7.29
K ₂ O	0.00	0.09	0.23	0.29	0.10	0.41	0.02	0.23
Total	98.60	100.09	96.38	96.64	100.68	99.73	100.03	100.66
Si	9.334	9.705	10.645	10.545	9.648	10.116	10.488	10.571
Ti	0.000	4.420	3.504	3.542	0.001	0.007	0.000	0.079
Al	6.600	0.009	0.002	0.000	6.255	5.821	5.446	5.289
Fe ²⁺	0.114	0.265	0.025	0.023	0.100	0.083	0.028	0.166
Ca	2.627	2.835	2.095	2.161	2.403	1.826	1.544	1.313
Na	1.380	1.251	3.098	3.213	1.608	2.135	2.558	2.524
K	0.000	0.022	0.058	0.073	0.023	0.095	0.005	0.052
Total	20.056	18.507	19.427	19.556	20.038	20.082	20.070	19.994
%An	65.53	69.03	39.91	39.68	59.53	45.03	37.59	33.77
%Ab	34.41	30.40	59.01	58.99	39.88	52.61	62.30	64.89
%Or	0.07	0.56	1.08	1.33	0.59	2.36	0.11	1.34

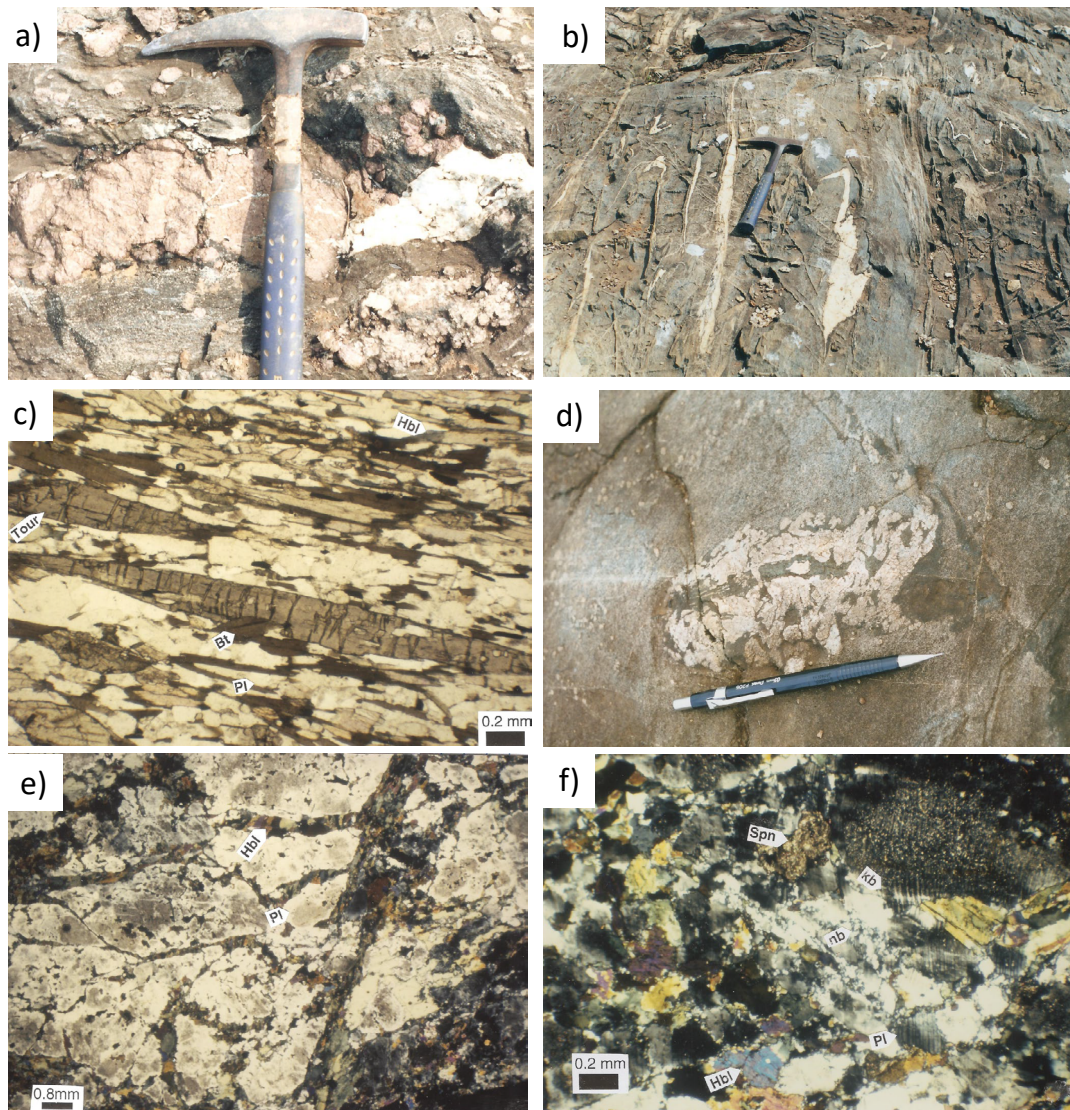
Continue...

Table 4. Continuation.

Nematoblastic amphibolites (inner aureole)										
	CAP 3 i	CAP 3 c	CD 5 i	CD 5 c	CD 5 c	CAP 15 c	CAP 15 c	CD 20 c	CD 20 i	CD 20 c
SiO ₂	57.24	55.98	58.59	59.18	59.43	55.67	53.24	59.47	61.99	59.36
Al ₂ O ₃	27.24	28.07	25.96	26.27	25.80	23.39	23.74	25.67	24.52	25.45
TiO ₂	0.04	0.00	0.00	0.01	0.00	0.00	0.00	0.00	0.00	0.00
FeO	0.04	0.00	0.00	0.00	0.14	0.01	0.00	0.12	0.00	0.21
MnO	0.06	0.00	0.00	0.00	0.00	0.01	0.09	0.00	0.05	0.03
MgO	0.00	0.00	0.00	0.00	0.00	0.01	0.01	0.00	0.00	0.01
CaO	9.22	10.71	7.68	7.53	7.80	9.11	11.28	7.54	4.95	7.73
Na ₂ O	5.95	5.40	7.37	7.12	7.08	8.62	7.36	7.51	8.78	7.45
K ₂ O	0.08	0.07	0.11	0.13	0.09	0.33	0.35	0.08	0.25	0.08
Total	99.92	100.29	99.82	100.25	100.35	97.22	96.08	100.40	100.55	100.32
Si	10.266	10.045	10.503	10.529	10.573	10.416	10.148	10.583	10.942	10.586
Ti	0.005	0.000	0.000	0.001	0.000	0.000	0.000	0.000	0.000	0.000
Al	5.758	5.936	5.484	5.508	5.410	5.158	5.333	5.383	5.100	5.349
Fe ²⁺	0.006	0.000	0.000	0.000	0.021	0.002	0.000	0.018	0.000	0.031
Ca	1.772	2.059	1.475	1.435	1.487	1.826	2.303	1.437	0.936	1.477
Na	2.069	1.879	2.561	2.456	2.442	3.127	2.720	2.591	3.004	2.576
K	0.018	0.016	0.025	0.030	0.020	0.079	0.085	0.018	0.056	0.018
Total	19.893	19.934	20.048	19.959	19.953	20.608	20.588	23.030	20.039	20.037
%An	45.91	52.07	36.31	36.61	37.63	36.29	45.09	35.51	23.42	36.29
%Ab	53.62	47.51	63.05	62.63	61.85	62.14	53.24	64.03	75.18	63.29
%Or	0.47	0.01	0.64	0.76	0.52	1.57	1.67	0.47	1.41	0.43
	CAP 26 i	CAP 26 c	CRN 32 r	CRN 32 c	CN 39 r	CN 39 c				
SiO ₂	57.60	55.98	56.52	53.27	54.82	53.16				
Al ₂ O ₃	26.77	27.09	27.69	29.97	25.91	28.76				
TiO ₂	0.00	0.00	0.00	0.00	0.01	0.01				
FeO	0.21	0.04	0.09	0.00	0.04	0.05				
MnO	0.00	0.00	0.03	0.14	0.00	0.01				
MgO	0.00	0.00	0.01	0.02	0.00	0.01				
CaO	8.44	9.39	10.67	13.06	10.41	12.56				
Na ₂ O	6.93	6.10	5.71	4.36	6.03	4.37				
K ₂ O	0.10	0.03	0.06	0.08	0.03	0.07				
Total	100.07	98.68	100.78	100.95	97.43	99.00				
Si	10.325	10.185	10.100	9.584	10.169	9.723				
Ti	0.000	0.000	0.000	0.000	0.001	0.001				
Al	5.655	5.809	5.832	6.354	5.664	6.199				
Fe ²⁺	0.031	0.006	0.013	0.014	0.006	0.008				
Ca	1.621	1.830	2.043	2.517	2.069	2.461				
Na	2.408	2.152	1.978	1.521	2.169	1.550				
K	0.023	0.007	0.014	0.018	0.007	0.016				
Total	20.063	19.989	19.980	20.008	20.085	19.959				
%An	40.00	45.88	50.63	62.06	48.74	61.12				
%Ab	59.44	53.94	49.03	37.49	51.09	38.48				
%Or	0.56	0.18	0.34	0.45	0.17	0.41				

c: core; i: intermediate; r: rim.

- *Conjugated veins and fractures* occur in metabasites from the inner aureole (Fig. 6E) and also in some xenoliths (Fig. 6D). The conjugate planes are steeply dip to 100–110° and 280–290°. The spacing of the fracture planes varies from 5 to 10 cm;
- *Banded veins*. Amphibolites may be crosscut by alternating and parallel veins of plagioclase and veins of amphibole so that a conspicuous banding is developed (Fig. 6E). When these parallel veins are prominent and strongly deformed, the outcrop displays a zebra aspect;
- *Hydraulic fractures with various directions* (Fig. 6F) occur in large numbers in amphibolites located to the north of the Estrela Granite Complex, where the country rocks form a concavity near the plutons 1 and 3 (Fig. 2);



Pl: plagioclase; Hbl: hornblende; Bt: biotite; Spn: sphene; Tour: tourmaline; nb: neoblasts of plagioclase; kb: kink band on plagioclase.

Figure 6. (A) Foliated garnet-biotite amphibolite from the inner aureole. Note the garnet porphyroblast and quartz aggregates (CAP3). (B) The same outcrop from the previous photo displaying folded quartz-bearing veins, veins parallel to the schistosity, and conjugate fractures (CAP3). (C) Photomicrograph (parallel polarizers) of foliated garnet-biotite amphibolite showing tablet-of-chocolate texture in tourmaline (CAP3). (D) Amphibolite crosscut by plagioclase + amphibole aggregate (CAP9). (E) Photomicrograph (crossed polarizers) showing a detail from the previous photograph. Plagioclase aggregate crosscut by narrow amphibole-bearing veins. (F) Detail from the previous photomicrograph (crossed polarizers) displaying kink bands and neoblasts.

Table 5. Summary of rock types, mineralogy, mineral chemistry, textures and temperature estimating. Domain

	Minerals	Amphibole chemistry	Structures	Textures	Temperature °C
Outer aureole	Actinolite, chlorite, epidote; plagioclase, magnetite	Low Al, Fe, Ti, K	Massive in metabasalts and metagabbros	Blastophitic; contrasted zoning in amphibole; skeletal magnetite	300–400
Transition	Actinolite; ferro pargasite; plagioclase biotite, magnetite	Low to moderate Al, Fe, Ti, K	Massive or weakly foliated	Coexistence of blastophitic texture with initial preferred orientation	400–500
Inner aureole	Ferro pargasite, plagioclase, ± biotite, ilmenite	High Al, Fe, Ti, K	Strong schistosity	Nematoblastic	550–630
Xenoliths	Ferro pargasite, ferro tschermakite, plagioclase, ± biotite, ilmenite	Al, Fe, Ti, K	Massive	Granoblastic	630–700

- *Centimeter-wide decimeter-long veins and fractures parallel to the S₂ schistosity* are common in the inner aureole. Several veins are filled with quartz and subordinate coarse-grained tourmaline. To the southeast of the Estrela Granite Complex, one can describe foliated garnet-biotite amphibolites that are characterized by abundant coarse-grained garnet porphyroblasts. Close to these garnet porphyroblasts, quartz veins and quartz aggregates are common (Fig. 5A). Some veins, emplaced orthogonally to the S₂ schistosity, are moderate to tightly folded (Fig. 5B);
- *Whitish-gray decimeter albite aggregates* are found within some foliated amphibolites from the inner aureole, to the north of the Estrela Granite Complex. These aggregates show a whitish-gray color and are composed of coarse-grained albite (Fig. 5D). These plagioclase portions are crosscut by narrow and erratic amphibole-bearing veins (Figs. 5D and 5E). Albite aggregates may occur parallel to the schistosity of foliated amphibolites. Plagioclase from these aggregates exhibits kink bands and fine-grained neoblasts along the contacts with amphibole veins (Fig. 5F). These deformation features are very similar to the mantle-and-core texture (cf. White 1975);
- *Decimeter- to meter-large quartz pockets* are hosted by foliated amphibolites. A significant example is the small Serra Verde gold deposit, where quartz is associated with pyrite, chalcopyrite, and amphibole megacrystals. Veins filled with coarse-grained amphibole are associated with the quartz pockets.

DISCUSSION

The metamorphic evolution of the country metavolcano-sedimentary rocks that host the 2.76 to 2.74 Ga synkinematic granites is marked by three conditions in a prograde context. Initially, a widespread seawater hydrothermal alteration of greenschist facies promoted pervasive hydration replacing magmatic clinopyroxene with actinolite ± chlorite ± epidote.

The second phase is related to regional subhorizontal shortening which has given rise to steeply dip decimeter-wide foliated domains in the supracrustal rocks under temperatures between 300 and 400°C. These brittle-plastic structures are printed only in the outcrops far from the 2.76 to 2.74 Ga synkinematic granites.

In the inner aureole, the amphibolites exhibit strong schistosity S₂ which, in general, is parallel to the foliation S₁ and to the major axes of the synkinematic granites. The parallelism between the foliation S₁ with the schistosity S₂ developed in the amphibolites from the inner aureole suggests that regional deformation, granitogenesis, and thermal metamorphism were coeval. Along the outer aureole, temperatures may have reached 400–500°C (albite-epitode hornfels facies). Hence, in the studied metabasic and amphibolites, these conditions are marked by the gap of miscibility of plagioclase (An < 10 to An > 17) and amphibole (actinolite to ferropargasite) in the transition conditions comparable with those of the greenschist to amphibolite facies (cf. Liou *et al.* 1974, Maruyama *et al.* 1983, Elmer *et al.* 2006).

Even taking into account the problems concerning the stability reached in low temperatures and the related chemical diffusion difficulties, one has tried to estimate the pressure of the country rocks during granite emplacement and thermal effects. The geobarometer amphibole-chlorite (Laird 1991), employed in metaultramafic schists that underwent low-grade metamorphism, furnished a pressure range from 2.2 to 3.1 kbar. Similar pressures were estimated through the calculations with the Thermocalc program, which was developed by Powell and Holland (1988). For pressure estimation, one has tested a garnet-biotite amphibolite (sample CAP 3). The average pressure is 3.36 ± 0.67 kbar, considering that the statistical requirements were attained (sigfit = 0.71, when the sigfit must be lower than 1.61). These pressure values agree well with the estimates done when amphibole compositions of the studied rocks are similar to the low-pressure amphiboles from the Abukuma type (cf. Laird and Albee 1981).

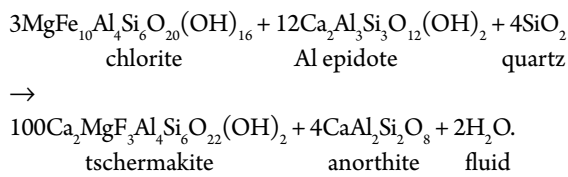
For the inner aureole, estimations were done with chemical analysis of a garnet-biotite amphibolite (sample CAP 3, Table 1). Based on the garnet-hornblende geothermometer (cf. Graham and Powell 1984) and on the assemblage plagioclase (An > 17) and ferropargasite, temperatures from 520 to 610°C (hornblende hornfels facies) were estimated. The set of independent reactions obtained with the THERMOCALC program is equivalent to 95% reliability for which the sigfit value must be lower than 1.73. The average temperature calculated is 629 ± 35 °C, considering the good statistical requirements (sqrt [MSWD] < 1.54; sigfit = 0.87).

Another temperature estimation of the inner aureole and xenoliths is based on the paragenesis plagioclase + ferropargasite + cummingtonite, which formed by the disappearance of epidote and chlorite. In foliated and massive amphibolites, according to Liou *et al.* (1974), the presence of ilmenite and the absence of chlorite indicate low oxygen fugacity conditions and temperatures higher than 550°C. Bucher and Grapes (2011) show that in low-pressure conditions (~ 3 kbar), plagioclase (An > 17), hornblende, and even clinopyroxene occur in lower temperatures compared with those of the regional metamorphism. In the amphibolite xenoliths, metamorphic clinopyroxene indicates temperature interval between 600 and 750°C (hornblende to pyroxene hornfels facies). This temperature interval is confirmed by the absence of orthopyroxene in the amphibolite xenoliths.

After hydration during seawater metamorphism, the metabasites from the Itacaiúnas Supergroup underwent contact metamorphism and plastic deformation during the emplacement of 2.76 to 2.74 Ga syntectonic granites (Estrela, Serra do Rabo, and Igarapé Gelado plutons). The inner aureole developed under 550 to 630°C, and the xenoliths recrystallized under the temperature of approximately 680°C. In these two domains, amphibole-bearing veins are widespread in amphibolites.

The increase in temperature due to contact metamorphism promoted dehydration reactions and progressive changes in amphibole chemistry. Reactions similar to those proposed by Cooper (1972) could have occurred in the amphibolites, both to explain OH- and silica releasing, increasing of fluid

pressures, and consequently the generation of hydraulic fractures and veins.



The brittle behavior of supracrustal country rocks changed when shallow-level (~3 kbar) syntectonic granites intruded (Barros *et al.* 2001, 2009). Aureole flattening associated with contact metamorphism and regional subhorizontal shortening created a thermal aureole deformed in plastic conditions, similar to the cases presented by Evans *et al.* (1998) and Morgan *et al.* (1998).

Lateral expansion stresses during the granite emplacement coeval with regional shortening produced the foliated amphibolites from the inner aureole. The increase in temperatures around the host supracrustal rocks has changed the rheological behavior in the inner aureole, which was plastically deformed. There, the rocks show a strong schistosity across approximately 2 km. Therefore, the strong mineral preferred orientation of these amphibolite rocks reflects the heating coeval with the inner aureole flattening. Considering thermal evolution, widespread dehydration reactions occurred within the inner aureole rocks and in metabasic xenoliths. In response to the high volatile production, the fluid pressures increased significantly and overcame the lithostatic pressure.

In the foliated amphibolites from the inner aureole, amphibole and plagioclase crystals show strong preferred orientation, rare intracrystalline deformation, and straight margins. These minerals can exhibit polygonal contacts. These textures indicate that pressure solution was the main recrystallization mechanism, which was followed by initial grain boundary area reduction. Mineral dissolution, when controlled by deformation, has been attributed to the increase of chemical potential on the crystal faces orthogonally with respect to the stress field (Vernon 1976, Bell and Cuff 1989). The role of the fluids, produced by dehydration reactions, is to enhance the transport of chemical components (Nakashima 1995) released by mineral dissolution. The transported components and the nature of the matter-filling veins will be controlled by the country rock composition involved in the tectono-metamorphic evolution. This could explain the large number of amphibole-bearing veins in the studied amphibolites. During the formation of nematoblastic and granoblastic textures, the rock framework may have the porosity progressively decreased and maintenance and cyclic increase in fluid pressure. This scenario was favorable to hydraulic fracturing and repeated production of veins. It is difficult to ascertain the amount of external fluids that could contribute to fluid pressure increase. It seems that most fluids were produced by dehydration reactions. However, some fluid could have also been furnished by granites.

Fractures and veins arranged in conjugate pairs or in tension gash position indicate coaxial components during the aureole deformation. Tightly folded veins formed in tension

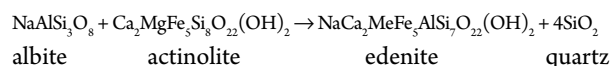
gashes, whereas the veins parallel to the schistosity were controlled by fluids channelized along the foliation. Where the amphibolites form a concavity to the north of the Estrela Granite Complex, numerous multidirectional hydraulic fractures seem to reflect a complex stress field. At that place, the WNW plutons would have imposed flattening striking NNE whereas the N-S pluton would have forced the wall rocks to W. Besides these stress directions related to the lateral expansion of granite plutons and aureole plastic deformation, the coeval regional NNE (Pinheiro and Holdsworth 1997, Barros *et al.* 2001) shortening also contributed to increasing the stress field complexity. As discussed by Brun and Pons (1981) and Brun *et al.* (1990), such coexisting forces resulted in areas of wholly constrictive strain. This complex stress field would have controlled the erratic distribution of the hydraulic fractures.

Another question that needs to be investigated is how very-coarse amphibole crystals formed in the veins. Taking into account the presence of a considerable volume of fluids released by dehydration reactions, nucleation and crystallization conditions would have been close to those expected in pegmatites. The low nucleation rate and high diffusion might result in few crystal nuclei so that coarse-grained crystals fill the veins. Simmons and Webber (2008) consider that, in pegmatite systems, slow cooling and crystallization enhance tabular or equant crystal shapes, different from the acicular crystals. In the studied amphibolites from the inner aureole and xenoliths, the fact that the veins are cyclic and filled by tabular equant amphibole crystals is coherent with the slow cooling of the host rocks in response to the effects produced by hot A-type granites. The garnet porphyroblast growth seemingly occurred in two steps. First, a syn-rotational garnet would have been formed during lateral expansion of the plutons. Hence, in some places, the heated inner aureoles experienced minor inverse movement in plastic conditions. After the main porphyroblast rotation, the residual regional flattening may have played a role together with the late thermal influence of the granites. At that time, the elongated garnet porphyroblasts had grown along the schistosity and wrapped the rounded crystals. It is another evidence of prolonged thermal effect and cooling of the wall rocks.

The size and shape of these amphibole crystals are very similar to the amphibole that fills the veins in neighboring gold mineralized domains (e.g., Serra Verde gold mine). Considering the temperatures in the inner aureole and xenoliths, the fluid production, and the dissolution of minerals, one could expect hot fluid migration which would be favorable to gold transport and ore-deposit origin.

Yardley and Botrell (1992) studied the relationship between metamorphism and veining and argued that silica solubility decreases with decreasing temperatures and pressures. Therefore, as fluid pressure decreases, in response to local space opening, Si-bearing volatiles precipitate to form veins and pockets. Those authors also discuss the silica origin and transport. Fluid distribution from the host rock throughout small distances and the migration of components could be enhanced by fluid advective and diffusion. To discuss the origin of quartz-bearing veins that crosscut the amphibolites, it

is necessary to compare the chemical composition of amphiboles. Actinolite formed during sweater metamorphism has lower contents of Ti, Al, and K when compared with the ferropargasite and ferrotschermakite that originated during contact metamorphism. The increase of Al observed in the higher-temperature amphiboles was accompanied Si decrease. The reaction proposed by Cooper (1972) would have occurred in the studied rocks and could explain the silica production during thermal metamorphism:



The presence of albite aggregates in amphibolites suggests that plagioclase also underwent some degree of dissolution during thermal effects and deformation. As the amount of albite pockets is by far less abundant when compared with amphibole-bearing veins, one could suggest that plagioclase was more resistant to dissolution than amphibole. Deformation of plagioclase close to thin amphibole veins is attributed (*cf.* Etheridge *et al.* 1984, McCaig and Knipe 1990) to the high temperature of the steam and the related increase in fluid pressure. The scape tendency of hot fluid would have been responsible for the intracrystalline deformation of plagioclase.

CONCLUSIONS

The metabasic rocks from the Itacaiúnas Supergroup underwent hydrothermal seawater alteration before contact metamorphism. Hot anhydrous granitic magmas, chemically comparable with the A-type granites, emplaced in shallow levels, synchronously to subhorizontal shortening. Plastic deformation during granite emplacement coeval with regional compressional stresses created thermal aureoles, which deformed in plastic conditions. Dehydration reactions coeval during

compressional stresses favored an increase in fluid pressure and hydraulic fracturing. The increased chemical potential induced the effective dissolution of minerals whose components were transported by volatiles. Replacement of actinolite by ferropargasite and ferrotschermakite released silica to fluids. It explains the presence of quartz veins in the amphibolites.

High volatile contents during veining created conditions similar to those present during pegmatite crystallization. Slow cooling in the inner aureole around granitic magmas favored the growth of coarse-grained and equant amphibole crystals filling most veins. Veins in a prograde metamorphism context, as that noticed in contact aureoles, might indicate places where matter transfer was effective. Heating and deformation of previously hydrated assemblages is one of the most propitious scenarios for fluid production, pressure solution mechanism, transfer of matter, and vein generation. Considering the mobility of chemical components expected in the metamorphic evolution of the synkinematic granites country rocks, veins and hydraulic fractures may represent interesting tracks for ore deposit prospecting in the Archean greenstone belts from the Carajás Province.

ACKNOWLEDGMENT

We thank the Universidade Federal do Pará, Universidade Federal do Paraná, University of Lorraine, and the Centre de Recherches Pétrographiques et Géochimiques (CRPG-CNRS) for the institutional support, financial resources, and analytical facilities. G. Queiroga thanks the Conselho Nacional de Desenvolvimento Científico e Tecnológico (CNPq) for the research council (Grant 430789-2016-5). We thank Prof. Pierre Barbey for his valuable comments. We are grateful to the Editors for the opportunity to present this article. We would like to thank Prof. Poliana Toledo and Bruna Borge Carvalho for the detailed text revision, precious comments, and suggestions.

ARTICLE INFORMATION

Manuscript ID: 20230035. Received on: 17 JUL 2023. Approved on: 24 APR 2024.

How to cite: Barros C.E.M., Queiroga G.N. (2024). Contact metamorphism and amphibole-bearing veins in Archean metabasic rocks from the Carajás Mineral Province, northern Brazil. *Brazilian Journal of Geology*, 54(2):e20230035. <https://doi.org/10.1590/2317-4889202420230035>

C.E.M.B.: Conceptualization, Data curation, Formal Analysis, Funding acquisition, Investigation, Methodology, Project administration, Resources, Software, Supervision, Validation, Visualization, Writing – original draft, Writing – review & editing. G.N.Q.: Methodology, Software, Supervision, Validation.

Competing interests: The authors declare no competing interests.

REFERENCES

- Almeida F.F.M., Hasui Y., Brito-Neves B.B., Fuck R.A. 1981. Brazilian structural provinces: an introduction. *Earth-Science Reviews*, 17(1-2):1-29. [https://doi.org/10.1016/0012-8252\(81\)90003-9](https://doi.org/10.1016/0012-8252(81)90003-9)
- Avelar V.G., Lafon J.M., Correia F.C. Jr., Macambira B.E.M. 1999. O magmatismo arqueano da região de Tucumã, Província Mineral de Carajás, Amazônia Oriental, Brasil: novos dados geocronológicos. *Revista Brasileira de Geociências*, 29:453-460.
- Barros C.E.M., Barbey P., Boullier A.M. 2001. Role of magma pressure, tectonic stress and crystallization progress in the emplacement of the syntectonic A-type Estrela Granite Complex (Carajás Mineral Province, Brazil). *Tectonophysics*, 343(1-2):93-109. [https://doi.org/10.1016/S0040-1951\(01\)00260-8](https://doi.org/10.1016/S0040-1951(01)00260-8)
- Barros C.E.M., Sardinha A.S., Barbosa J.P.O., Macambira M.J.B., Barbey P., Boullier A.M. 2009. Structure, petrology, geochemistry and zircon U/Pb and Pb/Pb geochronology of the synkinematic Archean (2.7 Ga) A-type granites from the Carajás Metallogenic Province, Northern Brazil. *The Canadian Mineralogist*, 47:1423-1440.
- Bateman R. 1985. Aureole deformation by flattening around a diapir during in-situ ballooning: the Cannibal Creek granite. *Journal of Geology*, 93:293-310.

- Beisiegel W.R., Bernardelli A.L., Drumond N.F., Ruff A.W., Tremaine J.W. 1973. Geologia e recursos minerais da Serra dos Carajás. *Revista Brasileira de Geociências*, **3**:215-242.
- Bell T.H., Cuff C. 1989. Dissolution, solution transfer, diffusion versus fluid flow and volume loss during deformation/metamorphism. *Journal of Metamorphic Geology*, **7**(4):425-447. <https://doi.org/10.1111/j.1525-1314.1989.tb00607.x>
- Bons P.D., Elburg M.A., Gomez-Rivas E. 2012. A review of the formation of tectonic veins and their microstructures. *Journal of Structural Geology*, **43**:33-62. <https://doi.org/10.1016/j.jsg.2012.07.005>
- Brun J.P., Gapais D., Cogné J.P., Ledru P., Vignerresse J.L. 1990. The Flamanville granite, (Northwest France): an unequivocal example of syntectonically expanding pluton. *Geological Journal*, **25**(3-4):271-286. <https://doi.org/10.1002/gj.3350250310>
- Brun J.P., Pons J. 1981. Strain patterns emplacement in a crust undergoing non-coaxial deformation, Sierra Morena, Southern Spain. *Journal of Structural Geology*, **3**(3):219-229. [https://doi.org/10.1016/0191-8141\(81\)90018-3](https://doi.org/10.1016/0191-8141(81)90018-3)
- Bucher K., Grapes R. 2011. *Petrogenesis of metamorphic rocks*. Springer-Verlag, 441 pp.
- Candela P.A. 1997. A review of shallow, ore-related granites: textures, volatiles, and ore metals. *Journal of Petrology*, **38**(12):1619-1633. <https://doi.org/10.1093/ptro/38.12.1619>
- Cesare B. 1994. Synmetamorphic veining: origin of andalusite-bearing veins in the Vedrette di Ries contact aureole, Eastern Alps, Italy. *Journal of Metamorphic Geology*, **12**(5):643-653. <https://doi.org/10.1111/j.1525-1314.1994.tb00048.x>
- Cooper A.F. 1972. Progressive metamorphism of metabasic rocks from the Haast Schist Group of Southern New Zealand. *Journal of Petrology*, **13**(3):457-492. <https://doi.org/10.1093/ptrology/13.3.457>
- Craveiro G.S., Villas R.N.N., Xavier R.P. 2019. Mineral chemistry and geothermometry of alteration zones in the IOCG Cristalino deposit, Carajás Mineral Province, Brazil. *Journal of South American Earth Sciences*, **92**:481-505. <https://doi.org/10.1016/j.jsames.2019.02.009>
- Dall'Agnol R., Cunha I.R.V., Guimarães F.V., Oliveira D.C., Teixeira M.F.B., Feio G.R.L., Lamarão C.N. 2017. Mineralogy, geochemistry, and petrology of Neoproterozoic ferroan to magnesian granites of Carajás Province, Amazonian Craton: The origin of hydrated granites associated with charnockites. *Lithos*, **277**:3-32. <https://doi.org/10.1016/j.lithos.2016.09.032>
- Dall'Agnol R., Lafon J.M., Macambira M.J.B. 1994. Proterozoic anorogenic magmatism in the Central Amazonian Province, Amazonian Craton: geochronological, petrological and geochemical aspects. *Mineralogy and Petrology*, **50**:113-138. <https://doi.org/10.1007/BF01160143>
- Davies S.R., Ferry J.M. 1993. Fluid infiltration during contact metamorphism of interbedded marble and calc-silicate hornfels, Twin Lakes area, central Sierra Nevada, California. *Journal of Metamorphic Geology*, **11**(1):71-88. <https://doi.org/10.1111/j.1525-1314.1993.tb00132.x>
- Docego 1988. Revisão litoestratigráfica da província mineral de Carajás. *Congresso Brasileiro de Geologia*, **35**, Belém. Província Mineral de Carajás: Litoestratigrafia e principais depósitos minerais. CVRD/SBG, 11-59.
- Dutrow B., Norton D. 1995. Evolution of fluid pressure and fracture propagation during contact metamorphism. *Journal of Metamorphic Geology*, **13**(6):677-687. <https://doi.org/10.1111/j.1525-1314.1995.tb00251.x>
- Elmer F.L., White R.W., Powell R. 2006. Devolatilization of metabasic rocks during greenschist-amphibolite facies metamorphism. *Journal of Metamorphic Geology*, **24**(6):497-513. <https://doi.org/10.1111/j.1525-1314.2006.00650.x>
- Etheridge M.A., Wall V.J., Cox S.F., Vernon R.H. 1984. High fluid pressures during metamorphism and deformation: implications for transport and deformation mechanisms. *Journal of Geophysical Research*, **89**(B6):4333-4358. <https://doi.org/10.1029/JB089iB06p04344>
- Evans N.G., Gleizes G., Leblanc D., Bouchez J. L. 1998. Syntectonic emplacement of the Maladeta granite (Pyrenees) deduced from relationships between Hercynian deformation and contact metamorphism. *Journal of the Geological Society*, **155**:209-216. <https://doi.org/10.1144/gsjgs.155.1.0209>
- Fabre S., Nédélec A., Poitras F., Strauss H., Thomazo C., Nogueira A. 2011. Iron and sulfur isotopes from the Carajás mining province (Pará, Brazil): Implications for the oxidation of the ocean and the atmosphere across the Archean-Proterozoic transition. *Chemical Geology*, **289**(1-2):124-139. <https://doi.org/10.1016/j.chemgeo.2011.07.019>
- Feio G.R.L., Dall'Agnol R., Dantas E.L., Macambira M.J.B., Santos J.O.S., Althoff F.J., Soares J.E.B. 2013. Archean granitoid magmatism in the Canaã dos Carajás area: Implications for crustal evolution of the Carajás province, Amazonian craton, Brazil. *Precambrian Research*, **227**:157-185. <https://doi.org/10.1016/j.precamres.2012.04.007>
- Fischer G., Fassbinder E., Barros C.E.M., Fossen H. 2019. The evolution of quartz veins during the tectonometamorphic development of the Brusque Metamorphic Complex, Brazil. *Journal of South American Earth Sciences*, **93**:174-182. <https://doi.org/10.1016/j.jsames.2019.04.027>
- Graham C.M., Powell R. 1984. A garnet-hornblende geothermometer: calibration testing and application to the Pelona Schist, Southern California. *Journal of Metamorphic Geology*, **2**(1):13-31. <https://doi.org/10.1111/j.1525-1314.1984.tb00282.x>
- Hanson R.B. 1992. Effects of fluid production on fluid flow during regional and contact metamorphism. *Journal of Metamorphic Geology*, **10**(1):87-97. <https://doi.org/10.1111/j.1525-1314.1992.tb00073.x>
- Hunger R.B., Xavier R.P., Moreto C.P.N., Gao J. 2018. Hydrothermal Alteration, Fluid Evolution and Re-Os Geochronology of the Grota Funda Iron Oxide Copper-Gold (IOCG) Deposit, Carajás Province (PA), Brazil. *Economic Geology*, **113**(8):1769-1794. <https://doi.org/10.5382/econgeo.2018.4612>
- Laird J. 1991. Chlorites: Metamorphic Petrology. In: Baily S.W. (ed.). *Hydrous Phyllosilicates (exclusive of micas)*. Reviews in Mineralogy 19. Michigan: Mineralogical Society of America, p. 405-453.
- Laird J., Albee A.L. 1981. Pressure, temperature, and time indicators in mafic schist: their application to reconstructing the polymetamorphic history of Vermont. *American Journal of Sciences*, **281**(2):127-175. <https://doi.org/10.2475/ajs.281.2.127>
- Leake B.E., Wolley A.L., Arps C.E.S., Birch W.D., Gilbert M.C., Grice J.D., Hawthorne F.C., Kato A., Kisch H.J., Krivovichev V.G., Linthout K., Laird J., Mandarino J.A., Maresch W., Nickel E.H., Rock N.M.S., Schumacher J.C., Smith D.C., Stephenson N.C.N., Ungaretti L., Whittaker E.J.W., Youzhi G. 1997. Nomenclature of Amphiboles: Report of the Subcommittee on Amphiboles of the International Mineralogical Association, Commission on new minerals and mineral names. *The Canadian Mineralogist*, **61**(405):295-310. <https://doi.org/10.1180/minmag.1997.061.405.13>
- Lindenmayer Z.G., Fyfe W.S., Laux J.H. 1994. Contribuição à Petrologia dos Metabasaltos do Grupo Salobo, Carajás, Pará. *Acta Geologica Leopoldensia*, **40**(17):115-152.
- Liou J.G., Kuniyoshi S., Ito K. 1974. Experimental studies of phase relations between greenschist and amphibolite in a basaltic system. *American Journal of Science*, **274**(6):613-632. <https://doi.org/10.2475/ajs.274.6.613>
- Macambira M.J.B., Lafon J.M. 1995. Geocronologia da Província Mineral de Carajás; síntese dos dados e novos desafios. *Boletim do Museu Paraense Emílio Goeldi, Ciências da Terra*, **7**:263-288.
- Machado N., Lindenmayer Z., Krogh T.H., Lindenmayer D. 1991. U-Pb geochronology of Archean magmatism and basement reactivation in the Carajás area, Amazon shield, Brazil. *Precambrian Research*, **49**(3-4):329-354. [https://doi.org/10.1016/0301-9268\(91\)90040-H](https://doi.org/10.1016/0301-9268(91)90040-H)
- Maruyama S., Suzuki K., Liou J.G. 1983. Greenschist-amphibolite transition equilibria at low pressures. *Journal of Petrology*, **24**(4):583-604. <https://doi.org/10.1093/ptrology/24.4.583>
- McCaig A.M., Knipe R.J. 1990. Mass transport mechanisms in deforming rocks: Recognition using microstructural and microchemical criteria. *Geology*, **18**(9):824-827. [https://doi.org/10.1130/0091-7613\(1990\)018<0824:MTMIDR>2.3.CO;2](https://doi.org/10.1130/0091-7613(1990)018<0824:MTMIDR>2.3.CO;2)
- Miller R.B., Paterson S.R. 1999. In defense of magmatic diapirs. *Journal of Structural Geology*, **21**(8-9):1161-1173. [https://doi.org/10.1016/S0191-8141\(99\)00033-4](https://doi.org/10.1016/S0191-8141(99)00033-4)
- Moreto C.P.N., Monteiro L.V.S., Xavier R.P., Amaral W.S., Santos T.J.S., Juliano C., Souza Filho C.R. 2011. Mesoarchean (3.0 and 2.86 Ga) host rocks of the iron oxide-Cu-Au Bacaba deposit, Carajás Mineral Province: U-Pb geochronology and metallogenetic implications. *Mineralium Deposita*, **46**:789-811. <https://doi.org/10.1007/s00126-011-0352-9>

- Moreto C.P.N., Monteiro L.V.S., Xavier R.P., Creaser R.A., Dufrane A., Tassinari C.C.G., Sato K., Kemp A.I.S., Amaral W.S. 2015. Neoproterozoic and Paleoproterozoic Iron Oxide-Copper-Gold Events at the Sossego Deposit, Carajás Province, Brazil: Re-Os and U-Pb Geochronological Evidence. *Economic Geology and the Bulletin of the Society of Economic Geologists*, **110**(3):809-835. <https://doi.org/10.2113/econgeo.110.3.809>
- Morgan S.S., Law R.D., Nyman M.W. 1998. Laccolith-like emplacement model for the Papoose Flat pluton based on porphyroblast-matrix analysis. *Geological Society of America Bulletin*, **110**(1):96-110. [https://doi.org/10.1130/0016-7606\(1998\)110<0096:LLEMFT>2.3.CO;2](https://doi.org/10.1130/0016-7606(1998)110<0096:LLEMFT>2.3.CO;2)
- Morimoto N., Fabries J., Ferguson A.K., Ginzburg I.V., Ross M., Seifert F.A., Zussman J., Aoki K., Gottardi G. 1988. Nomenclature of pyroxenes. *American Mineralogist*, **14**(5):198-221. <https://doi.org/10.2465/minerj.14.198>
- Nakashima Y. 1995. Transport model of buoyant metamorphic fluid by hydrofracturing in leaky rock. *Journal of Metamorphic Geology*, **13**(6):727-736. <https://doi.org/10.1111/j.1525-1314.1995.tb00255.x>
- Olszewski W.J., Wirth K.R., Gibbs A.K., Gaudette H.E. 1989. The age, origin and tectonic of the Grão-Pará Group and associated rocks, Serra dos Carajás, Brazil: Archean Continental volcanism and rifting. *Precambrian Research*, **42**(3-4):229-254. [https://doi.org/10.1016/0301-9268\(89\)90013-2](https://doi.org/10.1016/0301-9268(89)90013-2)
- Paterson S.R., Vernon R.H., Fowler Jr. T.K. 1991. Aureole systematics. In: Ribbe P.H. (ed.). *Contact Metamorphism*. Reviews in Mineralogy, **26**:673-722.
- Pidgeon R.T., Macambira M.J.B., Lafon J.M. 2000. Th-U-Pb isotopic systems and internal structures of complex zircons from an enderbite from the Pium Complex, Carajás Province, Brazil: evidence for the ages of granulites facies metamorphism and the protolith of the enderbite. *Chemical Geology*, **166**(1-2):159-171. [https://doi.org/10.1016/S0009-2541\(99\)00190-4](https://doi.org/10.1016/S0009-2541(99)00190-4)
- Pinheiro R.V.L., Holdsworth R. 1997. Reactivation of Archean strike-slip fault systems, Amazon region, Brazil. *Journal of the Geological Society of London*, **154**:99-103. <https://doi.org/10.1144/gsjgs.154.1.0099>
- Powell R., Holland T.J.B. 1988. An internally consistent thermodynamic dataset with uncertainties and correlations: 3: application methods, worked examples and a computer program. *Journal of Metamorphic Geology*, **6**(2):173-204. <https://doi.org/10.1111/j.1525-1314.1988.tb00415.x>
- Powell R., Holland T.J.B. 1994. Optimal geothermometry and geobarometry. *Journal of Metamorphic Geology*, **79**(1-2):120-133.
- Russ-Nabelek C. 1989. Isochemical contact metamorphism of mafic schist, Laramie Anorthosite Complex, Wyoming: Amphibole compositions and reactions. *American Mineralogist*, **74**(5-6):530-548.
- Sardinha A.S., Barros C.E.M., Krymsky R. 2006. Geology, geochemistry and U-Pb geochronology of the Archean (2.74 Ga) Serra do Rabo granite stocks, Carajás Metallogenic Province, northern Brazil. *Journal of South American Earth Sciences*, **20**(4):327-339. <https://doi.org/10.1016/j.jsames.2005.11.001>
- Schwarz M., Frantz J.C. 2013. Depósito de Cu-Zn Pojuca Corpo Quatro: IOCG ou VMS? *Pesquisas em Geociências*, **40**(1):5-19. <https://doi.org/10.22456/1807-9806.42425>
- Silva M.A.D., Monteiro L.V.S., Santos T.J.S., Moreto C.P.N., Sousa S.D., Faustini J.M., Melo G.H.C., Xavier R.P., Toledo, B.A.M. 2021. Mesoarchean migmatites of the Carajás Province: From intra-arc melting to collision. *Lithos*, **388-389**:106078. <https://doi.org/10.1016/j.lithos.2021.106078>
- Simmons W.B.S., Webber K.L. 2008. Pegmatite genesis: state of the art. *European Journal of Mineralogy*, **20**(4):421-438. <https://doi.org/10.1127/0935-1221/2008/0020-1833>
- Tallarico F.H.B., Figueiredo B.F., Groves D.I., Kositsin N., McNaughton N.J., Fletcher I.R., Rego J.L. 2005. Geology and Shrimp U-Pb Geochronology of the Igarapé Bahia Deposit, Carajás Copper-Gold Belt, Brazil: An Archean (2.57 Ga) Example of Iron-Oxide Cu-Au (U-REE) Mineralization. *Economic Geology*, **100**(1):7-28. <https://doi.org/10.2113/100.1.0007>
- Toledo P.I.F., Moreto C.P.N., Xavier R.P., Gao J., Matos J.H.S.N., Melo G.H.C. 2019. Multistage Evolution of the Neoproterozoic (ca. 2.7 Ga) Igarapé Cinzento (GT-46) Iron Oxide Copper-Gold Deposit, Cinzento Shear Zone, Carajás Province, Brazil. *Economic Geology*, **114**(1):1-34. <https://doi.org/10.5382/econgeo.2019.4617>
- Vignerresse J.L., Bouchez J.L. 1997. Successive granitic magma batches during pluton emplacement: the case of Cabeza de Araya (Spain). *Journal of Petrology*, **38**(12):1767-1776. <https://doi.org/10.1093/ptro/38.12.1767>
- Walther J.W., Orville P.M. 1982. Volatile Production and Transport in Regional Metamorphism. *Contributions to Mineralogy and Petrology*, **79**(3):252-257. <https://doi.org/10.1007/BF00371516>
- Wang L.G., McNaughton N.J., Groves D.I. 1993. An overview of the relationship between granitoid intrusions and gold mineralisations in the Archean Murchinson Province, Western Australia. *Mineralium Deposita*, **28**(6):482-494. <https://doi.org/10.1007/BF02431604>
- Weinberg R., Podladchikov Y. 1994. Diapiric ascent of magmas through power-law crust and mantle. *Journal of Geophysical Research*, **99**(B5):9543-9560. <https://doi.org/10.1029/93JB03461>
- White S. 1975. Deformation and recrystallization of oligoclase. *Contributions to Mineralogy and Petrology*, **50**:287-304. <https://doi.org/10.1007/BF00394854>
- Wirth K.R., Gibbs A.K., Olszewski W.J. 1986. U-Pb ages of zircons from the Grão-Pará group and Serra dos Carajás granite, Pará, Brazil. *Revista Brasileira de Geociências*, **16**(2):195-200.
- Yardley B.W.D., Botrell S.H. 1992. Silica mobility and fluid during metamorphism of the Connemara schists, Ireland. *Journal of metamorphic Geology*, **10**(3):453-464. <https://doi.org/10.1111/j.1525-1314.1992.tb00096.x>
- Yardley B.W.D., Cleverley J.S. 2015. The role of metamorphic fluids in the formation of ore deposits. *Geologic Society, London, Special Publications*, **393**:117-134. <https://doi.org/10.1144/SP393.5>